ACS OMEGA

http://pubs.acs.org/journal/acsodf

Article

Increasing the Strain Resistance of Si/SiO_2 Interfaces for Flexible Electronics

Tahereh Mohammadi Hafshejani, Ammar Mahmood, Jonas Wohlgemuth, Meike Koenig, Roberto C. Longo, and Peter Thissen*

Cite This: *ACS Omega* 2023, 8, 7555−7565

Read Online

ACCESS | Metrics & More | Article Recommendations

ABSTRACT: Understanding the changes that occur in the micro-mechanical properties of semiconductor materials is of utmost importance for the design of new flexible electronic devices, especially to control the properties of newly designed materials. In this work, we present the design, fabrication, and application of a novel tensile-testing device coupled to FTIR measurements that enables in situ atomic investigations of samples under uniaxial tensile load. The device allows for mechanical studies of rectangular samples with dimensions of 30 mm × 10 mm × 0.5 mm. By recording the alternation in dipole moments, the investigation of fracture mechanisms becomes feasible. Our results show that thermally treated SiO_2 on silicon wafers has a higher strain resistance and breaking force than the SiO_2 native oxide. The FTIR spectra of the samples during the unloading step indicate that for the native oxide sample, the fracture happened following the propagation of cracks from the surface into the silicon wafer. On the contrary, for the thermally treated samples, the crack growth starts from the deepest region of the oxide and propagates along the interface due to the change in the interface properties and redistribution of the applied stress. Finally, density functional theory calculations of model surfaces were conducted in order to unravel the differences in optic and electronic properties of the interfaces with and without applied stress.

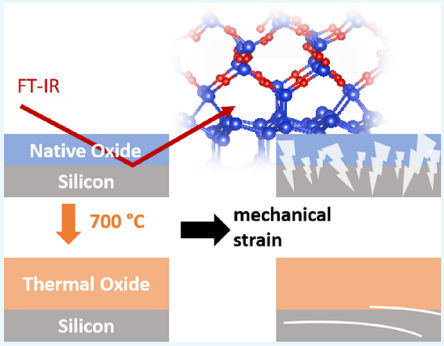

INTRODUCTION

The use of silicon as the main constituent of a new generation of microelectronic devices has prompted a renewed interest in the silicon research.[1−3] It is already well known that the growth of SiO_2 on the silicon surface is a fundamental reason for its electrical properties and structural stability. Due to some advantages such as lowering the overall package height profile and obtaining more functional devices per wafer unit area, decreasing the size of microelectronic circuits is still possible in the modern integrated circuit technology.[4] An emerging new field that is attracting considerable interest in the research community is the possibility of producing flexible electronic devices.[5] There are many existing applications for such materials, as implantable systems or portable devices.[6−8] Furthermore, the market for printed, flexible, and organic electronics is estimated to grow from $29.28 billion in 2017 to $300 billion by 2028. Therefore, research progress in flexible electronics is an exciting topic for both industrial and academic research.

Progress in flexible electronics research is driven basically by changes in size and shape at the microscale, which affects the basic properties drastically. For instance, Gupta et al. showed that the mechanical strength of ultrathin chips (UTC) is influenced by their thickness and the stress generated during the bending.[9] They revealed that the created stress is inversely proportional to the radius of curvature and is directly proportional to the thickness of UTC.

Many researchers have succeeded in obtaining the value of material parameters like the ultimate breaking strength. However, that does not solve fundamental questions related to the stress. For example, what is the mechanical mechanism creating degradation of the material in the external stress field? What is the effect of having different microstructures? Can an oxide act as a protective layer and how? Therefore, for the optimization of stress-including processes, monitoring the sample response under external forces at the atomic level is of fundamental importance.

In order to find a correlation between mechanical stress and reaction of the materials at the atomic scale, we designed and implemented our own device. Briefly, this device allows us to gradually increase the value of deflection on samples (under a three-point bending system) and simultaneously perform Fourier-transform infrared spectroscopy (FTIR) measure-

Received: October 25, 2022
Accepted: January 4, 2023
Published: February 14, 2023

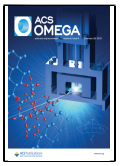

https://doi.org/10.1021/acsomega.2c06869
ACS Omega 2023, 8, 7555−7565

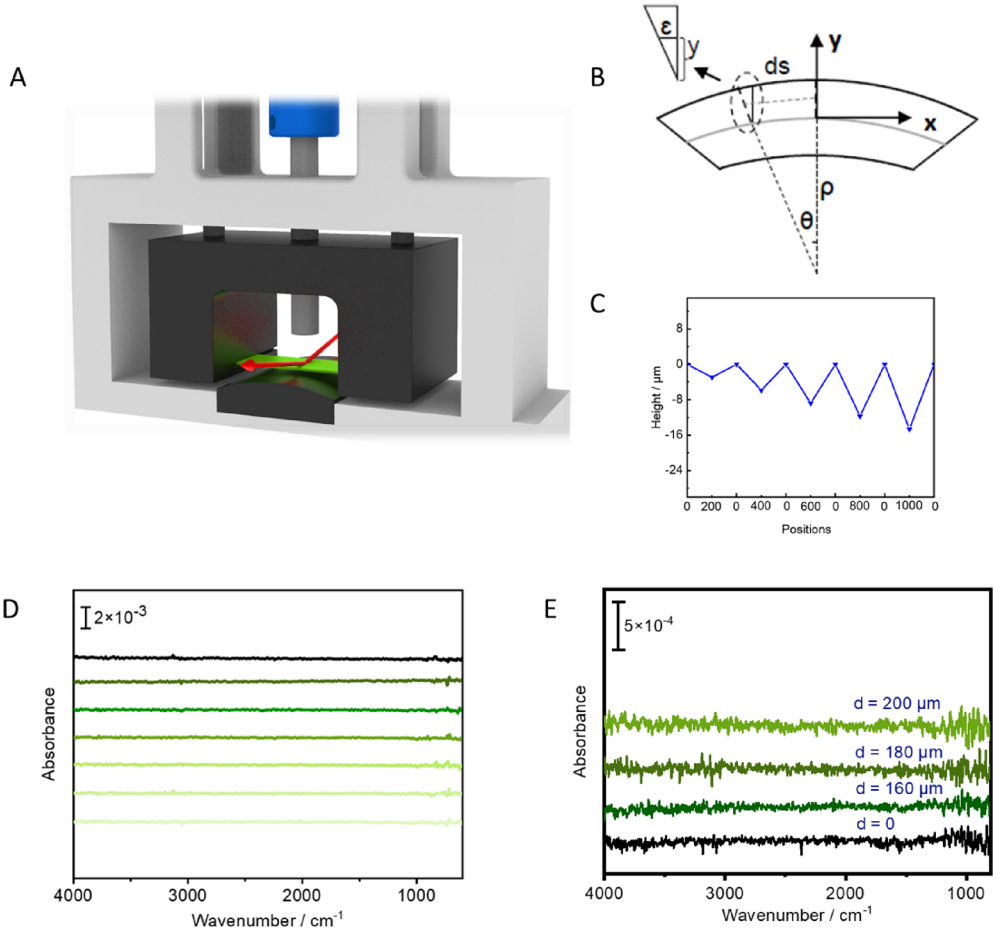

Figure 1. (A) Schematic illustration of our self-made instrument, which contains a stepper motor and spindle (blue color) as well as a movable sample holder (black color), an IR beam (red color), the sample (green color), and a nose-like metal piece (black color). (B) Schematic drawing of the relation between curvature radius, ρ, wafer curvature, and the strain within a wafer exposed to bending moments. (C) Graph showing the procedure of applying force on the sample in different positions (the number of positions equals the number of spindle steps). (D) IR reflection of a gold-coated aluminum sample bent by an amount equivalent to a 2.9 μm deflection in each step. (E) IR reflection spectra of HF-cleaned Si(111) in different deflections.

ments. The basic idea follows the work of Turek et al., who reported that mechanical stress can change the density of dipole moments and refractive index.[10] However, the mechanical device used in this work is remarkably different: we implemented a fully automatic three-point bending device with no friction and application of uniaxial loading. We intend to analyze the mechanisms behind long-lasting materials or study the possibility of having self-healing during synthesis.

The abovementioned changes in the size and shape of UTC can affect their properties and induce strain in the structure. It is well-known that there is no scattering to the carriers in a perfect periodic crystal. Any factor inducing changes to periodicity potentially introduces a scattering source, like charged and neutral impurities, dislocations, etc. Also, lattice thermal vibrations cause the fluctuation of the periodic potential, becoming another scattering source. The importance of this phenomenon is that these scattering sources (such as polar optical phonons in the SiO_2 layer) affect the mobility of the silicon carriers. Understanding the effects of strain on SiO_2 properties at the atomic scale is particularly important.

FTIR spectroscopy is a well-established technique for characterizing surfaces and adsorbate films. It provides specific information on the chemical composition and structure of thin surface layers and adsorbed molecules.[11−15] By using FTIR, we intend to elucidate whether external vibrational spectroscopy combined with a mechanical device can monitor the optical phonon modes in the SiO_2 layer and how strain affects these oscillator properties (such as oscillator density, height, and frequency). As the tendency in microelectronic devices is toward decreasing SiO_2 thickness or in general the size of the device, two silicon wafers with different oxide thickness are used. By performing a systematic stress-in situ FTIR spectroscopy study, we analyze in detail the surface Si-O_x vibrational modes, as they evolve from those associated to localized and well-characterized surface species to phonon-like modes associated to extended films.

Finally, we use density functional theory (DFT) to understand the effect of the interface structures on the electronic properties of the oxides under different stress conditions. Additionally, our calculations provide useful information regarding specific interfacial vibration modes and how they are affected by the strain and the bonding nature of each specific oxide/silicon model. Altogether, this work paves the road to systematic research on heterostructures for practical implementation in flexible electronic devices.

https://doi.org/10.1021/acsomega.2c06869
ACS Omega 2023, 8, 7555−7565

METHODS

Introduction to Our Self-Made Instrument. The device consists of a movable sample holder, moving toward a noise-like metal piece (see Figure 1A). The sample is placed inside a slot located in the sample holder.[16,17] The movable sample holder and the nose-like metal piece are connected through an open current circuit. When the sample encounters the nose-like metal piece for the first time, the circuit closes, which is defined as the zero position. It is worth noting that a full rotation of the stepper motor includes 51,200 equivalent steps. Each step in the motor results in a spindle rotation, implying a movable sample holder downward. After a full rotation of the stepper motor, the movable sample holder goes down to 0.75 mm. The number of steps and the value of the deflections were set by using LABVIEW written software.

After placing the sample in the zero position, the number of steps is increased in an orderly manner; for instance, the spindle turns 200 steps, which is equivalent to a 2.9 μm downward movement (deflection value). Then, FTIR measurements are performed, and the sample moves back to the zero position, where the next FTIR test is performed. Next, the spindle is turned 400 steps, equivalent to 5.8 μm (the entire procedure is shown in Figure 1C). This process is repeated and stopped using a computer-based program that controls the movable sample holder. It is important to note that the point of reflection (top inertia moment of the sample) does never change during the bending of the sample. To prove this, we repeat the measurement with a deflection of 2.9 μm on samples with complete reflectivity like gold-coated aluminum; the results are presented in Figure 1D. The obtained data reveal that alterations in the FTIR spectra result from the deformation of samples.[18,19]

The curvature radius ρ is calculated from the following equation:

$$\rho = \frac{x^2}{8d} \tag{1}$$

where x and d are the length of the sample (30 mm) and the deflection (μm) value at each position, respectively.[20]

Enhancing the value of the positions changes the curvature radius (ρ) (eq 1). Thus, by measuring ρ at each position, we can define the force as follows. We define E as Young's modulus of Si (165 = GPa),[21] ρ is the curvature radius at each position (mm), F is the applied force (GPa mm^2), d is the deflection (μm), and ε is the strain. I is called the moment of inertia ($I = \frac{bh^3}{12}$, where b and h are the width and thickness of the sample, respectively).

We use the Euler approximation to relate the bending moment with the deflection of samples ($\theta = \frac{\varepsilon}{y} = \frac{1}{\rho}$, $\rho \mathrm{d}\theta = \mathrm{d}s$, $\frac{\mathrm{d}y}{\mathrm{d}x} = \tan\theta$, Figure 1B). Furthermore, we use the small angle approximation ($\tan\theta \sim \theta$ and $\mathrm{d}s \sim \mathrm{d}x$) to describe the precise curvature of a bent wafer in intrinsic coordinates s and θ, relative to the position of the sample in Cartesian coordinates x and y:

$$\frac{1}{\rho} = \frac{\mathrm{d}\theta}{\mathrm{d}x} = \frac{\mathrm{d}^2y}{\mathrm{d}x^2} \tag{2}$$

Due to the Euler approximation, we can conclude

$$\frac{\mathrm{d}^2y}{\mathrm{d}x^2} = \frac{1}{\rho} = \frac{M}{EI} \tag{3}$$

The bending moment (M) is defined as

$$M = \frac{F}{2}x \tag{4}$$

By substituting M in eq 3, we have

$$\frac{\mathrm{d}^2y}{\mathrm{d}x^2} = \frac{Fx}{2EI},$$
$$\frac{\mathrm{d}y}{\mathrm{d}x} = \frac{Fx^2}{12EI} + c_1 \rightarrow y = \frac{Fx^3}{12EI} + c_1x + c_2 \tag{5}$$

In the following, the obtained parameter 'y' will be described as the deflection d (μm). The tensile stress developed during bending can be correlated to the bending moment. The stress in the wafer is a factor of the curvature radius of the sample and distance, y, from the neutral axis:

$$\frac{\mathrm{d}^2d}{\mathrm{d}x^2} = \frac{1}{\rho} = \frac{M}{EI} = \frac{Fx}{2EI} \tag{6}$$

After substituting $I = \frac{bh^3}{12}$ in the equation

$$\frac{\varepsilon}{d} = \frac{1}{\rho} = \frac{Fx}{2EI} \tag{7}$$

The strain formula is obtained as

$$\varepsilon = \frac{6Fxd}{Ebh^3} \tag{8}$$

Lastly, performing a stress calculation due to $\sigma = E\varepsilon$, we obtain

$$\sigma = \frac{6Fxd}{bh^3} \tag{9}$$

The basic idea behind investigating micro-mechanical properties using the FTIR spectra can be found in dichroism theory (see, e.g., ref 22). A vibrational, light-induced, transition between states i and j requires a change of dipole moments. For vibrational transitions, the dipole moment M_{ij} is defined as the change of dipole moment μ with the distance r between two atoms

$$\left(\frac{\partial\mu}{\partial r}\right)_{r_0} = M_{ij} \tag{10}$$

where r_0 is the equilibrium distance. It has been reported that the probability of transition and absorption is proportional to the square of the transition dipole moment:[22]

$$A \sim {M_{ij}}^2, \tag{11}$$

Here, we investigate the absorption coefficient of the samples through the reflection measurements using the experimental setup schematically shown in Figure 1A. The spectra dependence of the absorption is determined through the absorbance−wavenumber graph obtained using the following formula:

$$A = -\log\left(\frac{R}{R_0}\right), \tag{12}$$

https://doi.org/10.1021/acsomega.2c06869
ACS Omega 2023, 8, 7555−7565

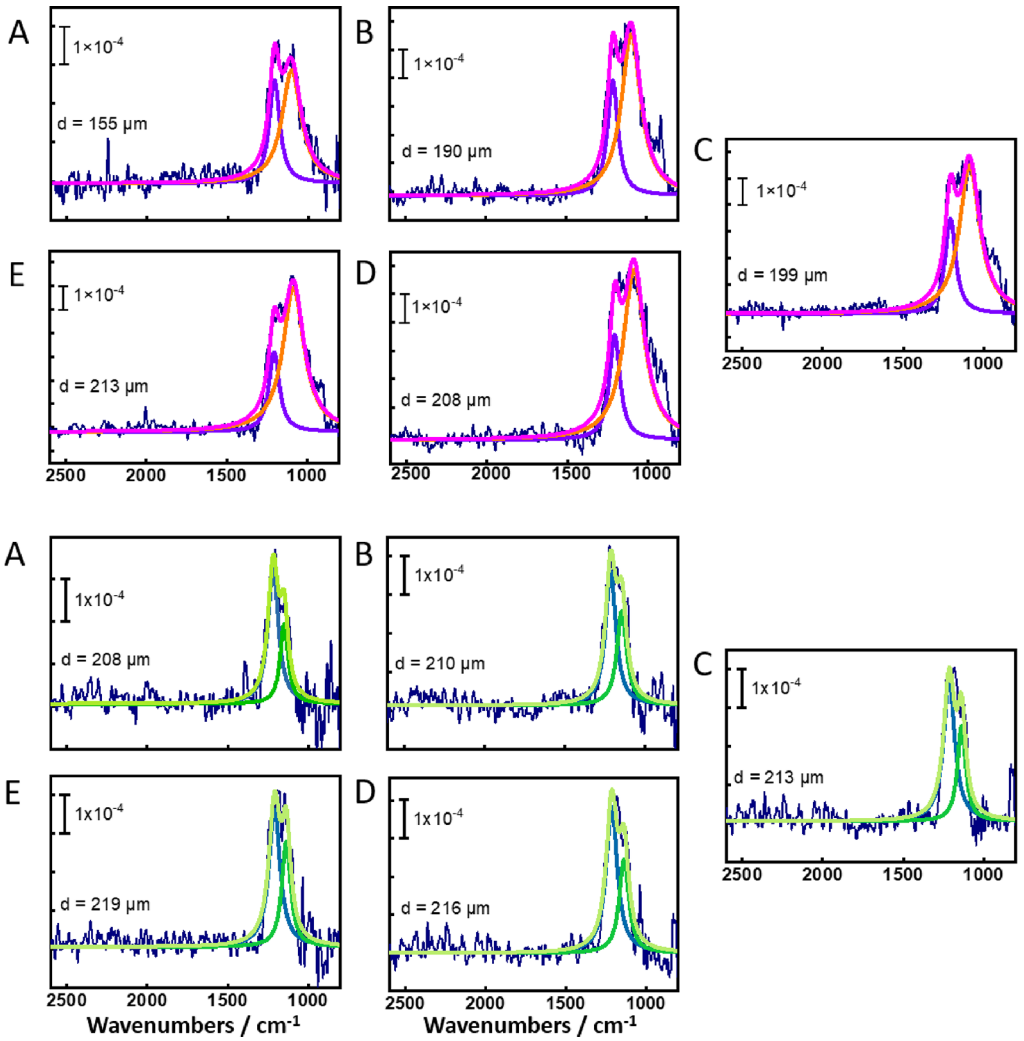

Figure 2. Upper panel images (A–E) depicting the FTIR spectra of the native oxide wafer in different bending positions. Deflection values are calculated from the number of steps included in each stepper motor rotation. Purple and orange lines result from the Lorentz fitting function. Bottom panel images (A–E) depicting the FTIR spectra of the thermal oxide wafer in different bending positions. Deflection values are calculated from the number of steps included in each stepper motor rotation. Blue and dark green lines result from the Lorentz fitting function.

where A is the absorbance and R_0 is the reflectance without bending.

Sample Preparation. Wafers of 3 cm × 1 cm × 500 μm CZ silicon(111) (N-type, phosphorus doped, resistivity of 24–34 Ωcm) and double-side polished are cleaned with 60 min exposure to deionized water at 60 °C and dried in a stream of nitrogen gas afterward. The samples are divided into two groups: the first set of samples is kept at room temperature (native oxide sample), while the other is oxidized at a temperature of 700 °C (thermal oxide sample) in an ambient atmosphere, resulting in various oxide thicknesses.

Fourier-Transform Infrared Spectroscopy (FTIR) Combined with Bending. FTIR measurements (spectra from 400 to 4000 cm^{-1}, reflection mode) with a VERTEX 70 were performed simultaneously by applying the force in different positions. Our self-made device was then used to apply a curvature on the samples placed into a N_2-purged glovebox.

Spectroscopic Ellipsometry (SE). SE measurements were performed using M2000 (Woollam Co., Inc., Lincoln, NE, USA). A two-layer optical box model was used to evaluate ellipsometry data for the silicon dioxide thickness. Values from the database implemented in the standard measurement software (CompleteEase, V5.19) were used to model the optical properties of silicon and silicon oxide.

Scanning Electron Microscope Analysis. The surface morphology of samples after bending was analyzed using the scanning electron microscope (SEM) Philips XL30 ESEM-FEG at 20 kV.0.

Computational Methods. DFT calculations were performed using the Vienna ab initio simulation package (VASP).[23] Most of the calculations were done using GPU accelerators,[24,25] which led to an increase in speed of almost 4-fold for some selected cases. Projector augmented wave (PAW) potentials were used to describe the electronic interactions.[26] The kinetic energy cutoff was set to 360 eV, and a 4 × 4 × 1 Monkhorst–Pack k-point mesh was used.[27] The approximation of electron–electron exchange and correlation energies was included via the generalized gradient approximation (GGA).[28] To account for dispersion forces, the DFT-D3 method by Grimme with Becke-Johnson damping function was used.[29,30] We determined that a setting of 4 × 4 × 1 k points yielded realistic electronic properties while keeping computation times reasonable. A relaxed Si(111) surface composed of four atomic layers passivated at the bottom by

https://doi.org/10.1021/acsomega.2c06869
ACS Omega 2023, 8, 7555–7565

Table 1. Data of the Best Obtained Fit to the Observed Peaks in the FTIR Spectra: Deflection (d), Position (υ), Full Width at Half Maximum (FWHM), and Height (H)

	native oxide				thermal oxide		
d/μm	υ/cm^{-1}	FWHM	H	d/μm	υ/cm^{-1}	FWHM	H
155	1208.2 ± 2.4	79.1 ± 8.8	3.5×10^{-4}	**208**	1213.8 ± 2.6	80.7 ± 8.2	3.6×10^{-4}
	1101.8 ± 4.3	145.9 ± 11.2	3.1×10^{-4}		1136.3 ± 3.8	49.2 ± 13.1	2.3×10^{-4}
190	1207.0 ± 0.0	78.9 ± 0.2	5.5×10^{-4}	**210**	1213.7 ± 0.0	83.9 ± 5.4	4.2×10^{-4}
	1091.8 ± 1.4	147.5 ± 0.1	5.9×10^{-4}		1136.3 ± 0.0	60.6 ± 7.1	3.2×10^{-4}
199	1205.0 ± 1.5	79.5 ± 0.1	5.3×10^{-4}	**213**	1213.3 ± 1.0	84.3 ± 0.4	4.0×10^{-4}
	1085.9 ± 1.0	155.1 ± 1.8	5.5×10^{-4}		1136.2 ± 0.1	62.1 ± 5.9	3.2×10^{-4}
208	1205.1 ± 0.0	79.7 ± 9.3	5.7×10^{-4}	**216**	1213.2 ± 0.6	84.2 ± 0.0	4.3×10^{-4}
	1084.9 ± 0.2	160.4 ± 1.5	5.6×10^{-4}		1136.5 ± 2.1	72.3 ± 6.2	3.3×10^{-4}
213	1204.3 ± 1.7	78.9 ± 6.5	5.1×10^{-4}	**219**	1208.1 ± 0.6	84.5 ± 0.8	4.1×10^{-4}
	1084.1 ± 1.9	160.1 ± 54	6.2×10^{-4}		1135.3 ± 2.5	66.7 ± 7.7	3.6×10^{-4}

hydrogen atoms was selected as the bulk system of the SiO_2/Si(111) interface, with an average surface atomic distance between neighboring silicon atoms of 3.8 Å. To compare the different interfacial atomic structures and their subsequent effect on vibrational properties, we constructed two models with the same SiO_2 thickness and different numbers of interface bonds. The supercell used in the calculations comprises 64 silicon atoms and 24 oxygen atoms (low interface density model, corresponding to the native oxide) and 64 silicon atoms and 28 oxygen atoms (high interface density model, corresponding to the thermal oxide). Additionally, each interface model was studied under different strain conditions. Tensile strains between 2 and 10% were applied to both in-plane supercell axes. For each case, atomic configurations were relaxed keeping the supercell volume fixed until the force acting on each atom was below 5×10^{-3} eV/Å. The eigenmodes and vibrational frequencies of the FTIR spectra were calculated using the force-constant approach, diagonalizing the mass-weighted second-derivative matrix (Hessian) for some selected Si−O bonds at the SiO_2/Si(111) interface. This restriction is reasonable because such eigenmodes do not overlap with those of the bulk-like Si(111) region.[1]

Radial Distribution Function. A radial distribution function (RDF) was used to determine the average interatomic distance between Si and O bonds for both the native and thermal oxide images (see Figure 3C,D). Equation 13 expresses the RDF $g(r)$ as a function of the local average density $\langle\rho(r)\rangle$ of radius r and the bulk density ρ.

$$g(r) = \frac{\langle\rho(r)\rangle}{\rho} \tag{13}$$

The local average density is defined in eq 14, where N_{avg} is the average total number of atoms surrounding an individual atom, which is then divided by the volume of a spherical shell, of thickness dr, encapsulating these atoms.

$$\rho(r) = \frac{N_{avg}}{4\pi r^2 \mathrm{d}r} \tag{14}$$

The bulk density is approximated using eq 15. Here, N_{total} is the total number of atoms inside a sphere of total radius equal to $(r + \mathrm{d}r)$.

$$\rho = \frac{N_{total}}{\frac{4}{3}\pi(r + \mathrm{d}r)^3} \tag{15}$$

The value of dr was kept fixed at 0.001 Å for the calculations of the RDF and was incrementally added to the radius r until the upper limit of 3.5 Å. A scan was performed at each radial step to determine the neighboring atoms. The Si−O bond was observed between 1.6 and 1.8 Å.

RESULTS AND DISCUSSION

Two types of samples with the same Si(111) substrate and different film thickness were used in this study. The film thickness was measured from the interference between the light reflected from the SiO_2 surface and the silicon substrate, using spectroscopic ellipsometry. Following the Deal−Grove model,[31] the silicon oxide layer grows via diffusion of oxidants toward the SiO_2/Si interface, where the reaction between the oxidizing agents (oxygen at the ambient atmosphere) with silicon occurs. The measured SiO_2 thickness for the silicon wafer at room temperature (without any thermal treatment) is 2.4 nm. After raising the temperature to 700 °C, the thickness increases to a value of 4.5 nm. This is an expected result given that the Arrhenius equation states that the diffusivity of oxygen through the oxide highly depends on the temperature.

An equivalent deflection was applied for all samples, starting at the zero position ($d = 0$) and increasing the deflection to 2.9 μm after a 200 step-turn of the spindle or 5.8 μm after the spindle is turned 400 steps. As explained in the Methods Section, each step (increasing the curvature on the sample) starts from the zero position. The applied force, strain, and stress at each curvature are then calculated using eqs 5, 8, and 9, respectively. In summary, silicon wafers are incrementally strained using this device, and the FTIR spectra are recorded at each strain level. FTIR spectroscopy allows us to collect information from a wide region of the samples due to the incident angle and the aperture radius. The pictures displayed in Figure 2 show the effect of the different deformation levels on the sample absorbance.

The deconvolution of the oxide absorbance band into elementary contributions is carried out using the Origin software. The band fitting program allows the use of reliable Lorentz profiles with little instrumental influence. Note that the Lorentz profile is not just a Cauchy function, but instead it is connected to the classical damped harmonic oscillator model and its corresponding dispersion relations. The absorption can be represented rather accurately by the sum of two symmetric Lorentzian profiles, with the corresponding maximum located at the oscillator position. The obtained data are presented in Table 1.

https://doi.org/10.1021/acsomega.2c06869
ACS Omega 2023, 8, 7555−7565

The vibrational properties of amorphous silicon dioxide are usually interpreted in terms of Si−O−Si subunits.[32] Broad FTIR spectra features in the 900−1300 cm^{-1} region are caused by asymmetrical stretching (AS) vibrations of bridging oxygen atoms. In the bending test, each deflection causes a strain, spread throughout the entire sample. Therefore, the stress value calculated for each deflection represents the overall values of stress in the sample. Table 2 shows the values of the external force, strain, and stress undergone by the samples during the presented deflection-FTIR results.

Table 2. Calculated Values of Deflection, Curvature, Force, Stress, and Strain

d (μm)	curvature (mm)	force (GPa mm^2)	stress (GPa)	strain
155	724.5	1.18×10^{-22}	0.145	0.0040
190	590.7	1.45×10^{-22}	0.219	0.0073
199	564.7	1.52×10^{-22}	0.240	0.0080
208	540.8	1.58×10^{-22}	0.261	0.0087
210	533.3	1.61×10^{-22}	0.269	0.0089
213	526.0	1.63×10^{-22}	0.276	0.0092
216	518.9	1.65×10^{-22}	0.284	0.0094
219	512.0	1.67×10^{-22}	0.292	0.0097

As shown in Figure 3A,B, the effect on the FTIR spectra is first observed at the deflections of 155 and 208 μm for native and thermal oxide, respectively. Our results clearly reveal that increasing the strain leads to quantizable modifications of the optical properties of SiO_2 films. Following the description provided in the Methods Section, one can state that increasing deflection changes the distance between atoms, which results in a modification in the density of dipole moments. The plots indicate that the deformation slightly enhances the absorbance magnitude (height value), while the wavenumbers of the corresponding peaks in each sample slightly shift to lower wavenumbers (Table 1).

The observed wavenumbers are in accordance with those presented in previous studies on amorphous SiO_2. For instance, Kirk et al. showed that, for amorphous SiO_2 in the 900−1400 cm^{-1} range, there are two types of lattice-vibrational modes, each exhibiting some LO-TO frequency splitting.[33,34] The most prominent vibrational mode, in-phase asymmetric stretching (AS1, the adjacent oxygen atoms move in-phase with each other), exhibits a TO mode at a frequency of approximately 1076 cm^{-1} and an LO mode at a frequency of around 1256 cm^{-1}. A second vibrational mode, out-of-phase asymmetric stretching (AS2, adjacent oxygen atoms are 180° out of phase), is located in between the AS1 LO-TO pair frequencies and exhibits a TO mode at ∼1200 cm^{-1} and an LO mode at ∼1160 cm^{-1}. Marta et al. also showed that there are three vibrational modes with TO-LO phonon splitting in the 900−1300 cm^{-1} spectra region of amorphous SiO_2.[35] Their reported peaks in the AS spectra region are 1072, 1207, and 1248 cm^{-1} for LO phonons, paired with 1164, 1228, and 1063 cm^{-1} TO modes, respectively. Additionally, Tian et al. reported two absorbance features characterizing the oxide spectra: a TO band at 1000−1150 cm^{-1} and an LO band at 1200−1260 cm^{-1}.[36,37]

The first band for the native oxide sample is observed at a stress of 0.145 GPa or a strain value of 0.0040. The obtained wavenumbers of 1208.2 and 1101.8 cm^{-1} can be assigned to LO and TO phonon modes. Since their frequency distance is larger than that of a LO-TO splitting, each mode can be treated independently. For the thermal oxide sample, two modes at higher wavenumbers of 1213.8 and 1136.3 cm^{-1} for a strain of 0.0087 were detected. These peaks can be related to the AS2 vibration in amorphous SiO_2, indicating an LO-TO splitting (LO mode at 1136.3 cm^{-1} and TO mode at 1213.8 cm^{-1}). The parameters of these peaks agree well with those of ref 37. The different atomic density of the native oxide and the thermal oxide likely results in a modification of the distance between Si dangling bonds and the interacting atoms in the oxide layer. For the oxide layer with lower atomic density (native oxide), a Si dangling bond shows larger bonding distance with the oxygen atoms of the oxide layer or other Si atoms, resulting in an isolating silicon dangling bond state. On the other hand, for the higher atomic density oxide layer (thermal oxide), a Si or oxygen atom in the oxide layer is

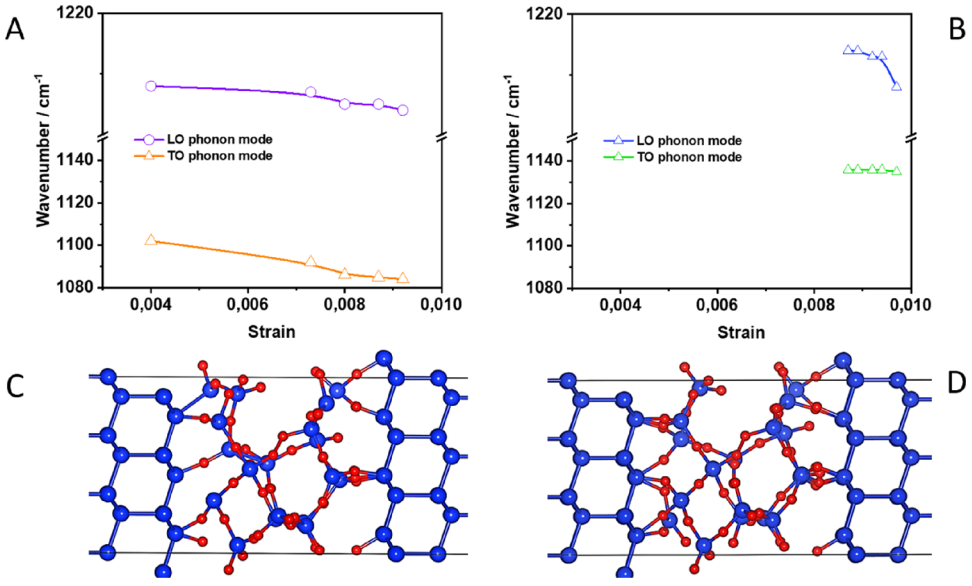

Figure 3. FTIR spectra of the native oxide (A) and the thermal oxide (B) as a function of the strain. Periodic interface atomic models for the native (C) and the thermal oxide (D). Silicon atoms are depicted in blue and oxygen in red.

https://doi.org/10.1021/acsomega.2c06869
ACS Omega 2023, 8, 7555−7565

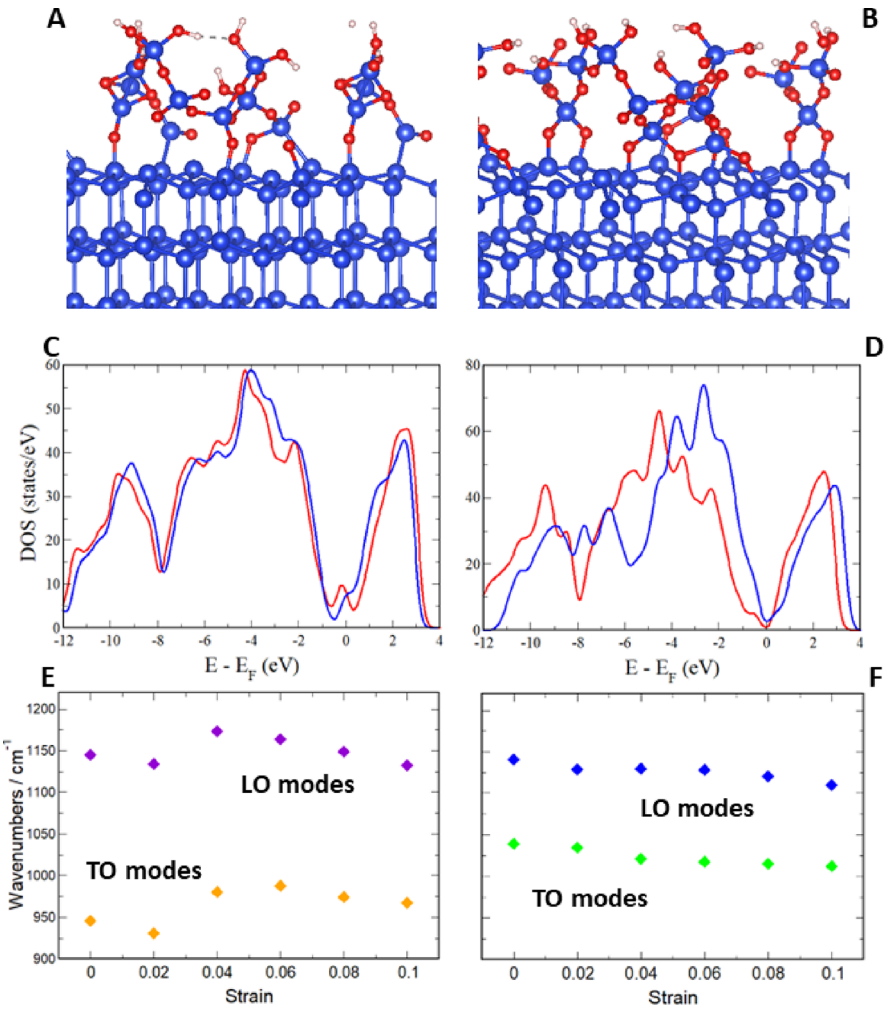

Figure 4. Upper panel: native oxide (A) and thermal oxide (B) interface models. Silicon atoms are depicted in blue, oxygen in red, and hydrogen in white. Medium panel: DOS for the pristine (red curve) and 6%-strained (blue curve) native oxide (C) and thermal oxide (D) interface models. FTIR spectra as a function of the strain for the native oxide (E) and thermal oxide interface models (F).

present near the Si dangling bond, with which they interact weekly. Therefore, a higher value of wavenumbers is obtained for the thermal oxide sample, which is expected to show a denser SiO_2 layer.

The set of strain effects on the peak positions of the FTIR spectra displays negligible redshift characteristics of phonon modes for both samples. For the thermal oxide, the frequency remains unchanged for both modes, and redshift is observed only for the TO mode of the unmodified wafer. For instance, the frequency of 1101.8 cm^{-1} obtained for a deflection of 208 μm decreases to 1084.10 cm^{-1} for a 213 μm deflection value (the redshift is only 17 cm^{-1}). As shown in Table 1, the larger damping (FWHM) for native oxide samples (especially the TO mode) may be due to the larger lowering of symmetry due to a higher degree of disorder compared to the thermal oxide samples. The intensity of modes in both samples shows the same trend, higher with increasing strain, because strain effectively lengthens Si−O bonds, thus affecting the dipole moment density. The area below each curve corresponds to the oscillator density. Our results show that for the native oxide sample at a deflection of 155 μm, values of 0.033 and 0.066 are obtained for LO and TO modes. For the LO band, such a value slightly increases to 0.042 for a deflection of 213 μm; however, strain increases the density of the TO mode to 0.150 for a deflection of 213 μm. For the thermal oxide sample, density variations for TO and LO phonon modes are obtained in the range of 0.043−0.047 and 0.012−0.030, respectively, for deflections in the range of 208−219 μm.

As mentioned above, in this work we used DFT calculations to model the electronic structure and some selected frequencies of the FTIR spectra. Figure 4A,B shows the interface models for the native oxide and the thermal oxide. As can be noted from the pictures, the density of Si−O interface bonds is two times larger for the thermal oxide than that of the native oxide interface model, which is an attempt to reproduce the interfacial differences arising from heating the samples to 700 °C and the subsequent oxygen diffusion toward the Si bulk. Besides Si−O bonds, there are also direct Si−Si bonds in the native oxide model, which are absent from the thermal oxide model due to larger oxygen interdiffusion toward the interface. The difference in the electronic structure between both interface models can be neatly observed in the density of states (DOS), shown in Figure 4C,D for the native and thermal oxide models, respectively. Interestingly, the larger amount of interfacial Si−O bonds of the thermal oxide model results in a much more effective Si/SiO_2 interface reconstruction, which leads to the opening of a small band gap. On the contrary, the existence of Si dangling bonds in the native oxide model leads

https://doi.org/10.1021/acsomega.2c06869
ACS Omega 2023, 8, 7555−7565

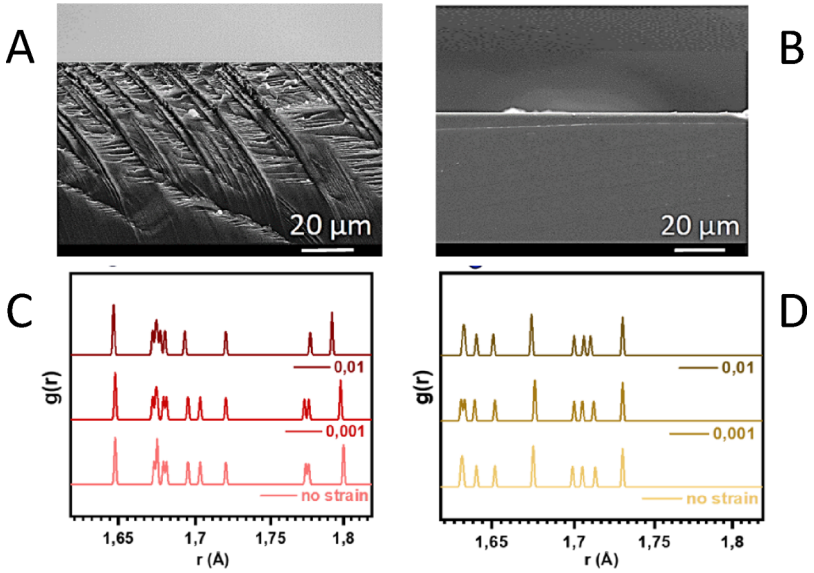

Figure 5. Upper panel: SEM image of the native oxide sample, showing crack propagation from the interface into the silicon (A). SEM image of the thermal oxide sample, indicating crack propagation parallel to the interface (B). Lower panel: radial distribution function of the native (C) and thermal oxide (D) interface models as a function of the strain.

to the formation of interface states, resulting in a non-semiconducting character. This is a conclusion of general validity, regardless of the specific interface models designed. As expected, the valence band maximum (VBM) and conduction band minimum (CBM) are formed in both cases by Si p and O p states. Figure 4C,D also displays the DOS upon applying a tensile strain of 6%. It can be seen that the effect on the thermal oxide DOS, although at first glance not remarkable, is of considerable importance. Indeed, the slope of the VBM is steeper, which reduces the dispersion, therefore increasing the carrier velocity. For the native oxide interface model, the application of a tensile strain shifts the interface states toward the CBM, thus forming a *p*-junction. Although both conclusions need to be strictly considered within the interface models used in the calculations, they can also be considered of general validity.

DFT calculations of the FTIR spectra were also performed for the native and thermal oxide interface models, at their equilibrium ground state and following the application of in-plane tensile strain. The results agree well with our experiments, showing little to no effect on the obtained wavenumbers. The reasoning of stress redistribution is also perfectly valid for the DFT calculations, given that both interface models have 2−3 SiO_2 oxide layers; therefore, an outward relaxation can absorb a tensile stress by elongating the interfacial Si−O bonds. Such elongation oscillates from 1−5% for the range of strains considered in this work (2−10%) and is non-uniform. For instance, for two neighboring Si−O interface bonds of 1.64 Å length in the thermal oxide model, the application of a tensile strain of 6% increases their length to 1.68 and 1.85 Å, depending on the availability of Si−O pairs. More isolated Si−O pairs redistribute the strain more effectively, as discussed below. Figure 4E,F shows the wavenumbers as a function of the strain for the native and thermal oxide models, in the same region of the FTIR spectra obtained in our experiments. Indeed, the pictures show no relevant redshift with the application of the strain. The largest differences are obtained for the TO modes of the native oxide model, approximately 50 cm^{-1}. The LO-TO frequency difference for the thermal oxide is around 100 cm^{-1}, a bit larger to be considered splitting, but in agreement with our experimental results. For the native oxide model, such a difference increases to 200 cm^{-1}, larger than in our experiments.

Reasons for such discrepancies are difficult to infer, but they can be attributed to the difficulty of capturing all the bond differences in a scarcely populated Si/SiO_2 interface. The overall magnitude of the frequencies obtained is also slightly lower than that of our experiments, but that is a well-known DFT artifact. LO modes correspond primarily to single AS1 vibrations whereas TO modes are more related to AS2 collective displacements. Interestingly, the FTIR spectra of the native oxide interface model peaks at a strain of 4%, smoothly decreasing further. We can then conclude by saying that our DFT results agree with the experimental trends in showing little effect in the FTIR spectra with tensile strain, due to a smooth reconstruction of the interfacial Si−O bonds.

Our experimental setup is highly lean on sensitivity due to the low reflectivity of dielectric substrates. That might be one of the motives that prevented us from detecting other well-known peaks of SiO_2 films in the obtained FTIR spectra. Additional steps like using the narrow-band mercury cadmium telluride detector might improve the obtained spectra, but that will be the subject of further research. Furthermore, there might also be a proximity effect on infrared vibrations due to the silicon substrate. Indeed, infrared active vibrations are basically an electronic phenomenon since they arise from the motion of charged atoms. The proximity of free carriers in the silicon substrate might affect the vibrational frequency of SiO_2 modes.[38] This can be effectively discarded using in situ FTIR on a silicon wafer with no SiO_2 film. The native oxide on the Si wafer was chemically cleaned with a 30 min exposure at 80 °C to a 1:3 solution of aqueous H_2O_2 and conc. H_2SO_4. The wafer was then rinsed with DI water and dried under a steady stream of nitrogen. The Si(111) was H-terminated by a 30 s dip in aqueous 49% HF followed by a 2.5 min dip in aqueous 49% NH_4F and a careful rinse with DI water to remove any trace of fluoride. This procedure formed a ⟨111⟩-oriented surface, H-

https://doi.org/10.1021/acsomega.2c06869
ACS Omega 2023, 8, 7555−7565

terminated, and atomically smooth over hundreds of nanometers. The results show that the obtained FTIR peaks are not caused by proximity to the silicon substrate (see Figure 1E).

There are two differences between the native and the thermal oxide worth mentioning. First, the thickness of the SiO_2 for the treated sample is almost twice than that of the non-treated sample. The second difference implies the number of expected cracks. Indeed, such a number is expected to be larger for the thermally treated sample due to the cooling process from 700 °C to room temperature. One might then ask the question of how increasing the thickness of SiO_2 results in larger resistance to higher forces and negligible effects in the FTIR spectra. The answer is that a thicker SiO_2 film involves larger number of bonds at the interface between the substrate and the film. In addition, a larger thickness leads to the formation of a more compact film. Therefore, in order to modify ρ and consequently increase the dipole moment, the thermal oxide sample should be bent more than the native oxide sample. Furthermore, an increase in the thickness and a change in the interface properties entail a redistribution of the stress across the sample and therefore an increase in the required force to achieve critical crack length. Here, redistribution means that the applied force is not only balanced by the bending moment but also by the tensile stress of the sample.[39]

The next relevant question that needs to be addressed is the absence of any effect in the FTIR of the thermally treated sample even close to the breaking force (high deflection). For this sample, the fracture mechanism is more likely induced by the transformation of more stress in the tip of located cracks in the deeper part of the wafer. Otherwise, there at least should be some evidence in the FTIR spectra because the measurements were performed in reflection mode, and they should show evidence of significant cracks on the surface when performing the tests in the zero position. On the other hand, the interface between SiO_2 and Si can redistribute the stress, thus counteracting any stress accumulation that might lead to a crack on the surface.[40] The interface should then be of brittle nature. At the end, a fracture may occur by debonding at the interface.

We then conclude that a thicker SiO_2 film increases the flexibility of the sample, which can tolerate larger external forces by changing the fracture mechanism. SEM images in Figure 5A,B show the differences in crack propagation across the samples. The pictures agree well with the FTIR spectra. The native oxide sample shows crack growth from the upper region of the interface, in the direction perpendicular to the applied force. For the thermal oxide sample, Figure 5B shows the presence of cracks parallel to the substrate which, upon increasing the mechanical stress, can propagate along the interface.

Figure 5D shows that the thermal oxide sample displays minor changes in the radial distribution function as a function of strain, whereas the native oxide sample shows some visible variations (see Figure 5C), and the average value of r, which represents the Si−O bond length, is overall larger. Using dichroism theory,[11] eq 10 states that the equilibrium distance (r_o) is directly proportional to the transition dipole moment (M_{ij}). Therefore, if Figure 5C shows a larger value of r_o (which is $r_{average}$, the bond length), that would lead to larger values of M_{ij}. Higher transition dipole moments lead to a larger absorbance intensity, as shown by the FTIR data in Table 1. On the other hand, Figure 5D displays the opposite scenario, where an overall lower $r_{average}$ leads to a lower equilibrium distance and therefore lower transition dipole moment. The relative peak shifts observed in Figure 5C,D allow us to conclude that the thermal oxide sample has larger integrity and that the native oxide sample shows lower integrity due to increased strain levels and major peak shifts (especially noticeable is the shift for the last peak, at 1.8 Å). The increased strain decreases the Si−O bond distance, which even results in a structure with missing peaks for the 0.01 strain level.

Our results clearly show that the SiO_2 film with increased flexibility and larger breaking force can be a good protector for the silicon wafer, especially under stress conditions. This is important for the fabrication of flexible electronic devices as performing deflection to produce bent wafers is essential. It is interesting to note that the effect of the thermal treatment on the production of cracks in the modified sample can be counteracted by the positive effect of having thicker SiO_2 films and a larger amount of bonds at the interface.

CONCLUSIONS

A new mechanical device combined with in situ FTIR spectroscopy was used to characterize the micro-mechanical behavior of silicon wafers with different SiO_2 films. We report the correlation between changes in the micro-structure and the optical properties of the samples. The FTIR spectra of the samples in a bent position clearly illustrate that, following deformation, the atomic distance gradually increases and intensifies the corresponding peak. Our results also reveal that the thermal oxide interface of SiO_2 enhances the flexibility and final breaking strength, also causing measurable changes in the optical characteristics. From the spectral curves of the samples in the un-loaded steps, two different fracture mechanisms were identified and further confirmed by SEM images taken from the samples' interface. The deformation of the native oxide led to the propagation of cracks from the surface. For the thermal oxide sample, the crack growth starts from the lower depth and propagates along the interface. Overall, this work aims at describing the application of in situ FTIR measurements within our own-made device to understand the micro-reaction of structures under mechanical stress. The final values of deflection, force, and stress are fully controllable; therefore, by adjusting the corresponding parameters, one can produce bent structures with interpretable optical properties.

AUTHOR INFORMATION

Corresponding Author

Peter Thissen − *Institut für Funktionelle Grenzflächen, Karlsruher Institut für Technologie, 76344 Eggenstein-Leopoldshafen, Deutschland; Institut für Massivbau und Baustofftechnologie, Abteilung Modellierung und Simulation, Karlsruher Institut für Technologie, 76131 Karlsruhe, Deutschland;* orcid.org/0000-0001-7072-4109; Email: peter.thissen@kit.edu

Authors

Tahereh Mohammadi Hafshejani − *Institut für Funktionelle Grenzflächen, Karlsruher Institut für Technologie, 76344 Eggenstein-Leopoldshafen, Deutschland*

Ammar Mahmood − *Institut für Massivbau und Baustofftechnologie, Abteilung Modellierung und Simulation, Karlsruher Institut für Technologie, 76131 Karlsruhe, Deutschland*

https://doi.org/10.1021/acsomega.2c06869
ACS Omega 2023, 8, 7555−7565

Jonas Wohlgemuth − *Institut für Funktionelle Grenzflächen, Karlsruher Institut für Technologie, 76344 Eggenstein-Leopoldshafen, Deutschland*

Meike Koenig − *Institut für Funktionelle Grenzflächen, Karlsruher Institut für Technologie, 76344 Eggenstein-Leopoldshafen, Deutschland;* orcid.org/0000-0003-3150-8723

Roberto C. Longo − *Tokyo Electron America, Inc., Austin, Texas 78741, United States;* orcid.org/0000-0003-4353-841X

Complete contact information is available at: https://pubs.acs.org/10.1021/acsomega.2c06869

Notes

The authors declare no competing financial interest.

■ ACKNOWLEDGMENTS

P.T. and T.M.H. acknowledge the DFG for financial support. The authors acknowledge funding from the Helmholtz Association.

■ REFERENCES

(1) Thissen, P.; Seitz, O.; Chabal, Y. J. Wet Chemical Surface Functionalization of Oxide-Free Silicon. *Prog. Surf. Sci.* **2012**, *87*, 272−290.

(2) Helms, C. R.; Poindexter, E. H. The Silicon-Silicon Dioxide System: Its Microstructure and Imperfections. *Rep. Prog. Phys.* **1994**, *57*, 791−852.

(3) Michalak, D. J.; Amy, S. R.; Aureau, D.; Dai, M.; Estève, A.; Chabal, Y. J. Nanopatterning Si(111) Surfaces as a Selective Surface-Chemistry Route. *Nat. Mater.* **2010**, *9*, 266−271.

(4) Teehan, P.; Kandlikar, M. Comparing Embodied Greenhouse Gas Emissions of Modern Computing and Electronics Products. *Environ. Sci. Technol.* **2013**, *47*, 3997−4003.

(5) Gao, W.; Ota, H.; Kiriya, D.; Takei, K.; Javey, A. Flexible Electronics toward Wearable Sensing. *Acc. Chem. Res.* **2019**, *52*, 523−533.

(6) Masoumi, S.; Zare, S.; Valipour, H.; Abdolhosseini Qomi, M. J. Effective Interactions between Calcium-Silicate-Hydrate Nanolayers. *J. Phys. Chem. C* **2019**, *123*, 4755−4766.

(7) Mohammadi Hafshejani, T.; Hohmann, S.; Nefedov, A.; Schwotzer, M.; Brenner-Weiss, G.; Izadifar, M.; Thissen, P. Formation and Stability of Nontoxic Perovskite Precursor. *Langmuir* **2019**, *35*, 16217−16225.

(8) Longo, R. C.; Cho, K.; Hohmann, S.; Thissen, P. Mechanism of Phosphorus Transport through Silicon Oxide During Phosphonic Acid Monolayer Doping. *J. Phys. Chem. C* **2018**, *122*, 10088−10095.

(9) Endler, S.; Hoang, T.; Angelopoulos, E. A.; Rempp, H.; Harendt, C.; Burghart, J. N.*In Mechanical Characterisation of Ultra-Thin Chips*, 2011 Semiconductor Conference Dresden, 27−28 Sept. 2011; 2011; pp. 1−4.

(10) Turek, I.; Tarjányi, N.; Martinček, I.; Káčik, D. Effect of Mechanical Stress on Optical Properties of Polydimethylsiloxane. *Opt. Mater.* **2014**, *36*, 965−970.

(11) Longo, R. C.; Schewe, N.; Weidler, P. G.; Heissler, S.; Thissen, P. Synthesis of Silicates for High-Performance Oxide Semiconductors: Electronic Structure Analysis. *ACS Appl. Electron. Mater.* **2021**, *3*, 299−308.

(12) Thissen, P.; Natzeck, C.; Giraudo, N.; Weidler, P.; Wöll, C. Hydration of Concrete: The First Steps. *Chemistry* **2018**, *24*, 8603−8608.

(13) Thissen, P.; Peixoto, T.; Longo, R. C.; Peng, W.; Schmidt, W. G.; Cho, K.; Chabal, Y. J. Activation of Surface Hydroxyl Groups by Modification of H-Terminated Si(111) Surfaces. *J. Am. Chem. Soc.* **2012**, *134*, 8869−8874.

(14) Szillies, S.; Thissen, P.; Tabatabai, D.; Feil, F.; Fürbeth, W.; Fink, N.; Grundmeier, G. Formation and Stability of Organic Acid Monolayers on Magnesium Alloy AZ31: The Role of Alkyl Chain Length and Head Group Chemistry. *Appl. Surf. Sci.* **2013**, *283*, 339−347.

(15) Izadifar, M.; Königer, F.; Gerdes, A.; Wöll, C.; Thissen, P. Correlation between Composition and Mechanical Properties of Calcium Silicate Hydrates Identified by Infrared Spectroscopy and Density Functional Theory. *J. Phys. Chem. C* **2019**, *123*, 10868−10873.

(16) Hafshejani, T. M.; Wohlgemuth, J.; Thissen, P. Strain Activation of Surface Chemistry on H-Terminated Si(111). *J. Phys. Chem. C* **2021**, *125*, 19811−19820.

(17) Hafshejani, T. M.; Feng, C.; Wohlgemuth, J.; Krause, F.; Bogner, A.; Dehn, F.; Thissen, P. Effect of Polymer-Coated Silica Particles in a Portland Cement Matrix Via in-Situ Infrared Spectroscopy. *J. Compos. Mater.* **2020**, *55*, 475−488.

(18) Szunerits, S.; Kirchner, C. N.; Wittstock, G.; Boukherroub, R.; Gondran, C. Electrochemical Investigation of the Influence of Thin Siox Films Deposited on Gold on Charge Transfer Characteristics. *Electrochim. Acta* **2008**, *53*, 7908−7914.

(19) Zawisza, I.; Wittstock, G.; Boukherroub, R.; Szunerits, S. Pm Irras Investigation of Thin Silica Films Deposited on Gold. Part 1. Theory and Proof of Concept. *Langmuir* **2007**, *23*, 9303−9309.

(20) Theron, C.; Mokoena, N.; Ndwandwe, O. M. Solid-State Compound Phase Formation of $TiSi_2$ Thin Films under Stress. *S. Afr. J. Sci.* **2009**, *105*, 440−444.

(21) Jaccodine, R. J. Surface Energy of Germanium and Silicon. *J. Electrochem. Soc.* **1963**, *110*, 524.

(22) Mayerhofer, T. G. Employing Theories Far Beyond Their Limits - Linear Dichroism Theory. *ChemPhysChem* **2018**, *19*, 2123−2130.

(23) Kresse, G.; Furthmuller, J. Efficient Iterative Schemes for Ab Initio Total-Energy Calculations Using a Plane-Wave Basis Set. *Phys. Rev. B* **1996**, *54*, 11169−11186.

(24) Hacene, M.; Anciaux-Sedrakian, A.; Rozanska, X.; Klahr, D.; Guignon, T.; Fleurat-Lessard, P. Accelerating Vasp Electronic Structure Calculations Using Graphic Processing Units. *J. Comput. Chem.* **2012**, *33*, 2581−2589.

(25) Hutchinson, M.; Widom, M. Vasp on a Gpu: Application to Exact-Exchange Calculations of the Stability of Elemental Boron. *Comput. Phys. Commun.* **2012**, *183*, 1422−1426.

(26) Kresse, G.; Joubert, D. From Ultrasoft Pseudopotentials to the Projector Augmented-Wave Method. *Phys. Rev. B* **1999**, *59*, 1758−1775.

(27) Monkhorst, H. J.; Pack, J. D. Special Points for Brillouin-Zone Integrations. *Phys. Rev. B* **1976**, *13*, 5188−5192.

(28) Perdew, J. P.; Burke, K.; Ernzerhof, M. Generalized Gradient Approximation Made Simple. *Phys. Rev. Lett.* **1996**, *77*, 3865−3868.

(29) Grimme, S.; Antony, J.; Ehrlich, S.; Krieg, H. A Consistent and Accurate Ab Initio Parametrization of Density Functional Dispersion Correction (DFT-D) for the 94 Elements H-Pu. *J. Chem. Phys.* **2010**, *132*, 154104.

(30) Grimme, S.; Ehrlich, S.; Goerigk, L. Effect of the Damping Function in Dispersion Corrected Density Functional Theory. *J. Comput. Chem.* **2011**, *32*, 1456−1465.

(31) Deal, B. E.; Grove, A. S. General Relationship for the Thermal Oxidation of Silicon. *J. Appl. Phys.* **1965**, *36*, 3770−3778.

(32) Queeney, K. T.; Herbots, N.; Shaw, J. M.; Atluri, V.; Chabal, Y. J. Infrared Spectroscopic Analysis of an Ordered Si/SiO_2 Interface. *Appl. Phys. Lett.* **2004**, *84*, 493−495.

(33) Comas-Vives, A. Amorphous SiO_2 Surface Models: Energetics of the Dehydroxylation Process, Strain, Ab Initio Atomistic Thermodynamics and IR Spectroscopic Signatures. *Phys. Chem. Chem. Phys.* **2016**, *18*, 7475−7482.

(34) Zhu, W.; Zheng, G.; Cao, S.; He, H. Thermal Conductivity of Amorphous SiO_2 Thin Film: A Molecular Dynamics Study. *Sci. Rep.* **2018**, *8*, 10537.

(35) Gunde, M. K. Vibrational Modes in Amorphous Silicon Dioxide. *Phys. B* **2000**, *292*, 286−295.
(36) Dai, M.; Kwon, J.; Halls, M. D.; Gordon, R. G.; Chabal, Y. J. Surface and Interface Processes During Atomic Layer Deposition of Copper on Silicon Oxide. *Langmuir* **2010**, *26*, 3911−3917.
(37) Tian, R.; Seitz, O.; Li, M.; Hu, W.; Chabal, Y. J.; Gao, J. Infrared Characterization of Interfacial Si−O Bond Formation on Silanized Flat Sio2/Si Surfaces. *Langmuir* **2010**, *26*, 4563−4566.
(38) Thissen, P.; Cho, K.; Longo, R. C. Nanopatterning of Group V Elements for Tailoring the Electronic Properties of Semiconductors by Monolayer Doping. *ACS Appl. Mater. Interfaces* **2017**, *9*, 1922−1928.
(39) Coletti, G.; Van Der Borg, N.; De Iuliis, S.; Tool, C.; Geerligs, L. Mechanical Strength of Silicon Wafers Depending on Wafer Thickness and Surface Treatment. *a, a* **2006**, *2000*, 86.
(40) Chan, K.; He, M.; Hutchinson, J. Cracking and Stress Redistribution in Ceramic Layered Composites. *Mater. Sci. Eng., A* **1993**, *167*, 57−64.

https://doi.org/10.1021/acsomega.2c06869
ACS Omega 2023, 8, 7555−7565